

# Faint 1.4 GHz sources in the 2dF Galaxy Redshift Survey

B.H.P. Chan<sup>1,\*</sup>, L.E. Cram<sup>1</sup>, E.M. Sadler<sup>1</sup>, N.E.B. Killeen<sup>2</sup>,  
C.A. Jackson<sup>2,3</sup>, B. Mobasher<sup>4</sup>, R.D. Ekers<sup>2</sup>.

<sup>1</sup>*School of Physics, A28, University of Sydney, NSW 2006, Australia*

<sup>2</sup>*Australia Telescope National Facility, CSIRO, Epping, NSW 1710, Australia*

<sup>3</sup>*Research School of Astronomy & Astrophysics, The Australian National University, Mount Stromlo Observatory, Canberra, Australia*

<sup>4</sup>*Space Telescope Science Institute, 3700 San Martin Drive, Baltimore, MD 21218, USA*

\**bchan@physics.usyd.edu.au*

8 November 2018

## ABSTRACT

The Australia Telescope Compact Array (ATCA) has been used to survey at 1.4 GHz, a small region ( $< 3$  sq deg) overlapping with the 2dF Galaxy Redshift Survey (Colless et al. 2001). We surveyed with a varying radio sensitivity, ranging from 1 mJy – 20  $\mu$ Jy ( $1\sigma$ ). There are 365 2dFGRS sources with  $z > 0.001$  lying within the surveyed region, of which 316 have reliable spectral classification. Following Sadler et al. (2002), we visually classified 176 as AGN or early-type galaxies, and 140 as star-forming galaxies. We derived radio flux density measurement or upperlimits for each of the 365 2dFGRS sources. The fraction of radio detected 2dFGRS star-forming galaxies increases from  $\sim 50\%$  at  $\sim 0.7$  mJy up to  $\sim 60\%$  at  $\sim 0.2$  mJy. The mean redshift for the fraction of radio detected star-forming galaxies increases with increasing radio detection sensitivity, while the mean redshift is fairly constant for the AGN/early-type fraction. We found very similar radio detection rates of 2dFGRS galaxies for both the AGN/early-type and star-forming components. The radio detection rate increases approximately linearly with respect to the rate of increase in radio detection sensitivity. We derived the radio luminosity function for our sample and it was found to be consistent with that of Sadler et al. (2002). We have also compared the total flux densities of NVSS sources common to our survey, and we discuss strategies for a large-scale radio survey of the 2dFGRS sample.

**Key words:** surveys – galaxies: statistics – galaxies: evolution – galaxies: distances and redshifts – galaxies: fundamental parameters – radio continuum: galaxies

## 1 INTRODUCTION

The decimetric synchrotron emission from galaxies is believed to arise from relativistic electrons accelerated by shock waves either in the interstellar medium, or in structures associated with an active galactic nucleus (AGN). In the former case, there is evidence that the decimetric luminosity is proportional to the rate of massive star formation, the link arising because supernovas are perhaps the dominant source of accelerating shock waves (Biermann 1976; Condon 1992). In the later case, the decimetric luminosity of an AGN may be related to the physical properties of the underlying black hole, and the rate and mode of mass accretion by that black hole (Franceschini, Vercellone & Fabian 1998; Laor 2000; Ho 2002).

Observations of the total decimetric luminosity of a galaxy thus allow an estimate of the extinction-free star-formation rate in galaxies where AGN emission can be con-

sidered negligible. Conversely, where the star formation rate is relatively low they provide information on the character of activity excited by a nuclear black hole. A few galaxies emit significant decimetric from combined nuclear star-formation and AGN activity (Hill et al. 2001; Veilleux 2001; Nagar et al. 2002).

The knowledge provided by radio flux density measurements is greatly enhanced when optical spectroscopic data are also available. Optical spectra reveal the galactic redshift, allowing the calculation of luminosities and hence estimates of the cosmic evolution of the rates of star-formation and black hole mass accretion. They also reveal the age and other properties of the most optically luminous components of the galactic stellar population and, in some cases, the state of excitement of a substantial fraction of the interstellar medium of the galaxy. Investigations of large galaxy samples having combined optical and radio data offer oppor-

arXiv:astro-ph/0310315v1 11 Oct 2003

tunities to address several outstanding astrophysical problems.

The 2dF Galaxy Redshift Survey (2dFGRS, Colless et al. 2001) has measured the optical spectra of over 220,000 galaxies photometrically selected to have an extinction-corrected magnitude brighter than  $b_J=19.45$ . The survey comprises strips at the equator, and near the South Galactic Pole (SGP). The SGP strip densely covers  $\sim 80^\circ \times 12^\circ$  ( $12^{\text{h}}40^{\text{m}} < \alpha < 03^{\text{h}}40^{\text{m}}$ ,  $-36.5^\circ < \delta < -24.5^\circ$ ), along with 99 randomly placed  $2^\circ$  (diameter) fields.

Sadler et al. (2002) studied the relatively bright radio sources among the 2dFGRS objects by cross-matching the 1.4 GHz NRAO VLA Sky Survey (NVSS, Condon et al. 1998) with the first  $\sim 20\%$  of the 2dFGRS. Approximately 1.5% of the 2dFGRS galaxies ( $\sim 5\%$  NVSS sources) have radio counterparts at the NVSS radio flux density detection limit of 2.8 mJy. Presumably, the majority of unmatched (95%) NVSS 1.4 GHz sources are AGNs whose optical counterparts are too faint to be detected at  $b_J=19.45$  (c.f. Condon 1988). Some 60% of the identifications are AGNs (radio galaxies and some Seyferts) and the remainder 40% comprised of star-forming objects. Sadler et al. (2002) note that complete cross-matching of the 2dFGRS and NVSS will provide approximately 4,000 radio source spectra, a sample large enough to measure radio galaxy evolution to  $z = 0.35$  and to locate the most luminous star-forming galaxies to  $z = 0.2$ . Condon et al. (2002) have reported evidence at the level of two standard deviations for evolution in the rate of star formation density between the mean redshifts,  $\langle z \rangle \sim 0.02$  and  $0.06$ , of their NVSS/UGC sample and the NVSS/2dFGRS sample of Sadler et al. (2002), respectively.

There is considerable interest in seeking radio identifications of 2dFGRS objects below the NVSS flux density limit. Spectroscopy of the optical counterparts of radio sources found in sub-mJy surveys (e.g. Benn et al. 1993; Georgakakis et al. 1999; Gruppioni, Mignoli & Zamorani 1999; Prandoni et al. 2001) suggests that the faint radio population will be a mixture of star-forming galaxies and AGNs, as it is for the mJy radio identifications. Interestingly, 1.4 GHz radio source counts rise sharply towards the Euclidean rate near 1 mJy (e.g. Condon 1988), a phenomenon ascribed to the rising proportion of star-forming galaxies in the sub-mJy population (Windhorst 1984; Condon 1988; Benn et al. 1993; Hopkins et al. 1998). In view of the tight correlation between radio and far infra-red (FIR) luminosity among the star-forming population, these galaxies likely correspond to the population of lower star formation rate ‘‘IRAS galaxies’’ seen at apparently brighter magnitudes. Studies of the sub-mJy counterparts of the 2dFGRS objects will thus encompass star-forming objects down to  $\sim 10^{22.5} \text{ WHz}^{-1}$  out to redshifts of  $z \sim 0.1$ , where evolution appears to have occurred, as well as AGNs of moderate radio luminosity.

The SGP part of 2dFGRS covers over 900 square degrees and would require a very large allocation of radio telescope time to undertake a co-extensive sub-mJy survey. Acknowledging this, we have undertaken a pilot study of a selected region of the 2dFGRS (equivalent area of one 2dFGRS-field), employing the Australian Telescope Compact Array (ATCA) at 1.4 GHz to explore probable outcomes and optimal observing strategies for a more extensive survey.

Section §2 describes the survey field selection, observations and data reduction and §3 the procedures used to derive radio flux measurements and radio upper limits of the 2dFGRS objects. §4 presents the radio luminosity function derived from our sample and comparison with that of Sadler et al. (2002). In §5 we explore the radio detection rate of 2dFGRS sources as a function of survey depth and in §6 we consider the optimisation of a full-scale sub-mJy survey.

Throughout the paper we have used  $\Omega_M = 1$ ,  $H_o = 70 \text{ km s}^{-1} \text{ Mpc}^{-1}$ , and adopted for all sources, a radio spectral index  $\alpha = -0.7$  ( $S \propto \nu^\alpha$ ).

## 2 SURVEY STRATEGY, FIELD SELECTION

One aim of this pilot survey is to investigate a survey strategy which yields optimal benefit from the ATCA observing time that would be invested in a deep, large-scale radio follow-up of the 2dFGRS. The basic trade-off lies between the steeply rising surface density of sources at fainter survey limits, versus the quadratic dependence of survey sensitivity on integration time. This implies a strategy in which a small area is surveyed very deeply, and a progressively larger area is surveyed to a progressively poorer sensitivity. Given the breadth of the total radio luminosity functions for both star-forming and AGN galaxies, and the weak dependence of the bi-variate radio luminosity function on optical luminosity, it would be hard to argue that any flux density range is to be preferred over any other, suggesting a strategy in which equal numbers of sources are detected to a progressively changing flux density limit.

Table 1 presents the results of calculations designed to illustrate this strategy. The Table uses the published sensitivity of the ATCA at 1.4 GHz using two 128 MHz IF channels, namely that a point source of  $S_{lim}$  mJy is detected at the field centre with  $5\sigma$  sensitivity in a time of  $(2.24/S_{lim})^2$  minutes, provided that full  $(u, v)$  coverage is obtained (ATCA on-line sensitivity calculator<sup>1</sup>). The Table relies on integral source densities read from Fig. 2(b) in Becker, White & Helfand (1995). According to the Table, a single pointing observed for 5,000 m (83 h) would reveal just over 3,000 sources per square degree, brighter than  $30 \mu\text{Jy}$ , and approximately the same number of sources would be detected to a  $5\sigma$  limit of 1 mJy if an area of 34 pointings was surveyed for a total of 170 m (3 h). These values are ideal estimate, excluding observation overheads. In practice, there are several other factors that must be considered in designing the survey. The limits given in the table refer to the most sensitive part of the primary beam, and can be approached to within a factor of about  $\sqrt{2}$  over a large area only if mosaicing techniques are exploited. Observations must be staged to provide adequate  $(u, v)$  coverage, and bright radio sources must be avoided to achieve high dynamic range.

Awarded  $8 \times 12$  hours of observation time for the pilot survey, we chose a mosaic of 16 pointings in square tessellation with a pitch of 17 arcmin. Embedded within the 16 pointing mosaic are sub-mosaics of 8, 4 and 2 pointings. Fig. 1 illustrates our mosaic pattern, where denser filling indicates a longer integration time at that pointing. This

<sup>1</sup> [http://www.atnf.csiro.au/observers/docs/at\\_sens/](http://www.atnf.csiro.au/observers/docs/at_sens/)

**Table 1.** Observing strategy.

(1)	(2)	(3)	(4)	(5)	(6)
Sensitivity ( $\mu\text{Jy}$ )	$1\sigma$ ( $\mu\text{Jy}$ )	time (min)	$N > S$ ( $\text{deg}^{-2}$ )	Relative area	Relative time
>1000	200	5	90	34	1
>316	63	50	275	11	3
>100	20	500	900	3.4	10
> 31	6	5000	3000	1	30

- (1) Point source  $5\sigma$  sensitivity.
- (2)  $1\sigma$  sensitivity.
- (3) Time to reach  $1\sigma$ .
- (4) Surface density of 1.4 GHz sources brighter than  $5\sigma$  limit.
- (5) Relative areas for equal source numbers.
- (6) Relative observing time for specified sensitivity and source numbers.

strategy is not a precise match to the data in Table 1, but it suffices to illustrate and explore it.

There are several requirements to consider in selecting the field. Firstly, it should lie away from strong sources ( $S \geq 100$  mJy), and be devoid of sources  $\geq 50$  mJy in the deepest region in order to achieve the desired sensitivity. The NVSS has been used to identify regions relatively free of strong sources. Secondly, it must lie within 2dFGRS and, for testing purposes, have at least 50% redshift completeness in the 100k 2dFGRS release (Colless et al. 2001). Finally, we note that the 2dFGRS SGP strip passes through the zenith of the ATCA (latitude  $-30^\circ 18' 52''$ ). Since mosaicing near the zenith results in large slew times for the alt-az mount, we choose to observe as far away from  $\delta \sim -30^\circ$  as possible.

Using these criteria we place the survey centre at  $\alpha = 23^{\text{h}} 37^{\text{m}} 35^{\text{s}}$ ,  $\delta = -27^\circ 52' 45''$  (J2000), coincident with the 2dF fields SGP192–SGP194 & SGP270–SGP272. Fig. 2 displays two adjoining NVSS mosaics (I2344M28 & I2328M28) showing the neighborhood of the target area. Annotated on this image are (i) large circles scaled to represent the 16 pointings of the 33 arcmin FWHM of the 1.4 GHz ATCA primary beam, (ii) small circles representing NVSS sources with  $50 \text{ mJy} \leq S < 100 \text{ mJy}$ , (iii) squares representing NVSS sources with  $100 \text{ mJy} \leq S < 150 \text{ mJy}$  and (iv) numbered squares representing NVSS sources with  $S \geq 150 \text{ mJy}$ . All NVSS sources with  $S \geq 50 \text{ mJy}$  lying within a  $2^\circ$  radius of the ATCA mosaic centre are marked in the image.

## 2.1 Observations and data reduction

Observations were performed over 8 days at the end of May 2001 with the ATCA in the 6F configuration. We used  $2 \times 128$  MHz IFs centred at 1344 MHz and 1432 MHz. Denoting the 16, 8, 4 and 2 pointing sub-mosaics as fields A, B, C and D, respectively, Table 2 list the average total integration time for each of these fields. To simplify observing programs, A-fields were observed only during a single  $1 \times 12$  h session, B-fields only in  $2 \times 12$  h sessions, C-fields in  $4 \times 12$  h sessions and D-fields observed in all 8 sessions.

To ensure good image quality, we need adequate  $(u, v)$  coverage. The 6 km array rotates to an independent  $(u, v)$

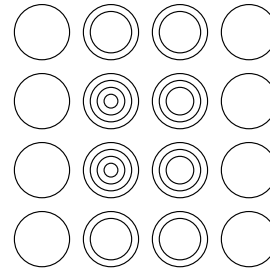


**Figure 1.** Illustration of mosaic pattern and survey depth, where each concentric circle groups represents individual pointing centres. In accordance with the denotation in §2.1, from lesser to denser filling circles indicating increase of total integration times corresponding to fields denoted A-fields up to D-fields.

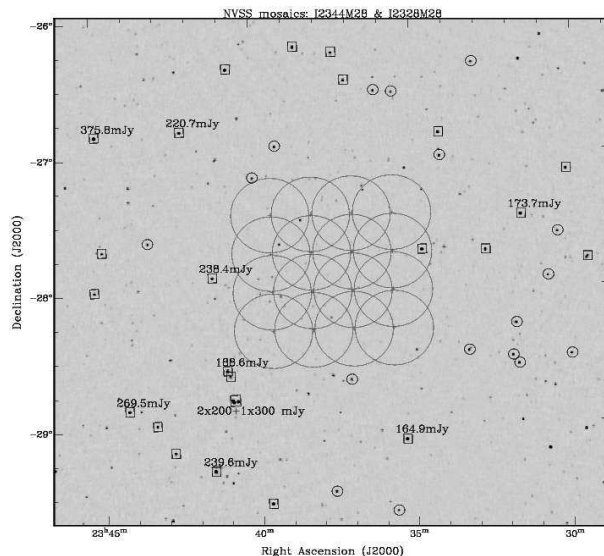


**Figure 2.** NVSS image. Large circles shows the pointings (FWHM) surveyed with the ATCA. We have marked all NVSS sources within a  $2^\circ$  radius of the ATCA mosaic centre having  $50 \text{ mJy} \leq S < 100 \text{ mJy}$  with small circles, and  $100 \text{ mJy} \leq S < 150 \text{ mJy}$  sources with small squares. Sources with  $S \geq 150 \text{ mJy}$  are explicitly indicated. The greyscale spans  $-10$  to  $40 \text{ mJy beam}^{-1}$ .

cell in about 80 s and ideally we would take two samples within this time. With 10 s integrations and the relevant slew times, this can be achieved only when mosaicing at most 4 pointings, especially since slew times increase for fields that transit near the zenith. Since we have 16 pointings in the A-fields, all obtained on a single day, they are under sampled. However the other fields are properly sampled since we have multiple days of observations to fill the  $(u, v)$  plane.

For primary calibration we used the ATCA standard PKS B1934-638, adopting  $S_{1384 \text{ MHz}} = 14.9 \text{ Jy}$  (Baars et al. 1977). For secondary calibration we have used B2331-240, adopting  $S_{1.5 \text{ GHz}} = 1 \text{ Jy}$  (Taylor 2002). The mosaic cadence is broken for secondary calibration every 40-50 m, scanning the calibrator for 2 m.

**Table 2.** Observation summary, with field-labels defined in §2.1, and illustrated in Fig. 1.

Field	$\tau^*$ (hr)	% flagged	$\sigma_T^\dagger$ ( $\mu\text{Jy}/\text{beam}$ )
A	0.45	8	105 (0.9K)
B	1.62	5	55 (0.5K)
C	6.32	5	28 (0.2K)
D	25.30	5	14 (0.1K)

\* Averaged integration time.

† Theoretical rms noise level and brightness temperature sensitivity.

### 2.1.1 Calibration and flagging

The 8 days of observations and each of the two IFs were reduced separately following the standard MIRIAD data reduction procedures:

(i) *Primary flux calibration:* The primary calibrator ( $u, v$ ) data set were flagged to remove bad ( $u, v$ ) samples and the gain, bandpass (MFCAL) and leakage (GPCAL) calibration tables were calculated using a 10 s solution interval.

(ii) *Secondary phase calibration:* As the target field was near the zenith there is limited coverage of parallactic angle for the secondary calibrator. Thus, the bandpass and leakage calibration tables from the primary calibrator are used (GPCOPY). The secondary calibrator ( $u, v$ ) data set were then flagged and the gain calibration determined (GPCAL) using a 10 s solution interval.

(iii) *Program source:* Calibration tables are copied to each of the program sources (pointings) from the secondary calibrator (GPCOPY) and each of the ( $u, v$ ) data sets flagged.

For our data flagging, we used the task TVCLIP developed by Prandoni et al. (2000) (see their §4.1). This allows the user to recursively flag a ( $u, v$ ) data set by specifying (i) a specific quantity from which a running median of the data sample is determined (e.g. amplitude of a polarisation) and (ii) a clip level, so that any ( $u, v$ ) data point exceeding the running median by more than the factor specified by the clip level will be flagged. We have found that deleting ( $u, v$ ) points having an amplitude greater than 10 times the running median removes typical interference. Where lower level interference persists we repeat the flagging procedure and remove all samples greater than 6 times the running median. Table 2 lists the averaged (all days and both IFs) percentage of data flagged for the field types defined in §2.1. The overall total amount of data flagged is 4.5%.

### 2.1.2 Imaging and self-calibration

Once the data are calibrated and interference is excised, we proceed to mosaicing. We have adopted a joint deconvolution approach with a Steer-Dewdney-Ito (SDI) CLEAN algorithm (Steer, Dewdney & Ito 1984) using the task MOSSDI2. This task is a version of MOSSDI modified by Regan et al. (2001) so that the CLEAN-cutoff level is expressed in terms of the locally determined image RMS instead of a fixed value in  $\text{Jy beam}^{-1}$ . This feature was very important in view of the large variation in the total inte-

gration time per pointing across the mosaiced region. We followed the basic MIRIAD joint-deconvolution procedures:

(i) Apply INVERT to the ( $u, v$ ) data of all pointings, both IFs (invoking options *mfs* to deal with bandwidth smearing) and all 8 days, with uniform weighting, 2 arcsec cell size, to generate a dirty mosaic and dirty beam cube (one dirty beam image per pointing).

(ii) Use MOSSDI2 to generate a joint-deconvolution CLEAN-component model of the dirty mosaic, CLEANing down to a specified CLEAN-cutoff level.

(iii) Use RESTOR to subtract the CLEAN component model, convolved with the appropriate dirty beam, from the dirty mosaic and then restore with an elliptical Gaussian profile fitted from the dirty beam.

(iv) Lastly, use MOSSEN to generate a gain image which then allows primary beam correction over the entire mosaic.

There are two artefacts evident in the mosaic. Firstly, weak positive and negative rings appear around strong sources, presumably reflecting amplitude calibration errors. The effect is largest for bright sources lying on the flank of the primary beam and is probably caused by pointing errors. There are also radial artifacts appearing as symmetric and asymmetric radial structures emerging from strong sources. These can be removed by phase self calibration. Comparison of our mosaics before and after the self calibration procedures, we found no spurious sources above  $3\sigma$  level, and source flux densities varies less than  $\sim 5\%$ , much smaller than the expected fitting uncertainty. The following summarises our imaging steps:

(i) Without restricting the CLEAN region deconvolve with MOSSDI2, CLEANing down to a CLEAN-cutoff level of  $10\sigma$  and generate a preliminary mosaic.

(ii) Use automatic source fitting of the preliminary mosaic to generate a list of CLEAN boxes over all fitted sources with peak flux density greater than 10 times the local image noise rms.

(iii) Generate a CLEAN component model for self-calibration using MOSSDI2, CLEANing over the boxes defined in (ii). Invoke the option *positive* to constrain the CLEAN components to be positive valued.

(iv) With the CLEAN components defined in (ii) investigate image quality improvement using various self-calibration solution intervals. Radial artifacts were completely removed for solution intervals lying between 10-30 s. We adopted 30 s to enhance the signal-to-noise ratio per self-calibration solution interval.

(v) With SELFCAL and a 30 s solution interval apply phase self-calibration to each pointing, each IF, and each day separately.

(vi) Using self-calibrated ( $u, v$ ) data, deconvolve with MOSSDI2 CLEANing down to  $5\sigma$  over CLEAN boxes defined in (ii). Use the new mosaic to define a new set of CLEAN boxes for all fitted sources with peak flux density greater than 5 times the local image noise rms. Finally generate a deep-CLEANed mosaic with MOSSDI2, CLEANing down to  $2\sigma$  over the new CLEAN boxes.

Displayed in Fig. 3 is the deep-CLEANed mosaic with an enlarged central portion. The contours represent  $1\sigma$  local image noise levels calculated in the manner described below. The 0.2 mJy noise contour in Fig. 3 corresponds closely to

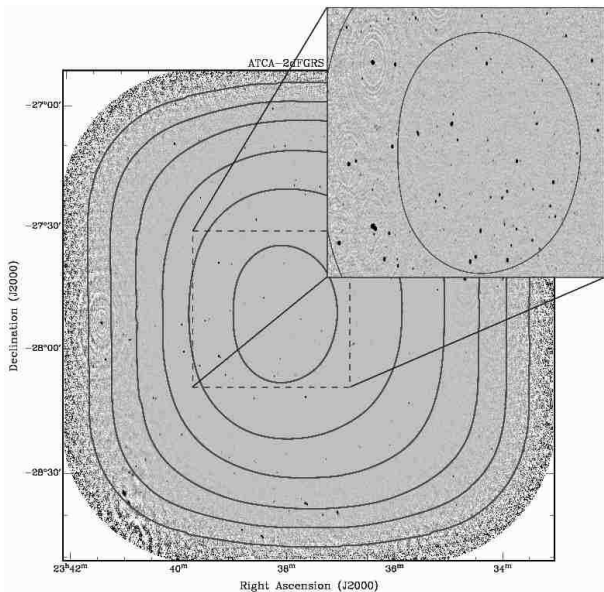


**Figure 3.** ATCA mosaic. The contours are drawn at the  $1\sigma$  noise level for 0.025, 0.05, 0.1, 0.2, 0.4 and 1 mJy. The greyscale is set to  $-1.5$  to  $4.5$  mJy beam $^{-1}$  for full the mosaic and  $-0.15$  to  $0.45$  mJy beam $^{-1}$  for the inset.

the outline of the 16-pointing mosaic region illustrated in Fig. 2. The synthesised beam size of the deep-CLEANed mosaic is  $15.5'' \times 8.0''$  at position angle  $1.20^\circ$ .

## 2.2 Local image noise estimate

It is important to estimate the local RMS noise for the image used in the source-fitting phase of our study. We could estimate the noise using RESTOR to form a residual image of the deep-CLEANed mosaic, but the estimate would exhibit irregular spatial variations. Instead we have generated a theoretical sensitivity image using MOSSEN, and checked the predictions using noise estimates based on 1000 randomly selected patches each  $\sim 3\times$  the synthesised beam area. The tight correlation between the prediction and the measured values shown in Fig. 4 is fit by  $\sigma = 10^{-0.06} \langle n \rangle^{0.97}$  with  $\sim 20\%$  uncertainty. This equation is used to scale the theoretical sensitivity image to estimate the local image RMS noise. Table 2 lists the theoretical RMS noise of the four field types defined in §2.1: the raw mosaic image RMS noise agrees with the predictions to within  $\pm 20\%$ .

## 3 RADIO DETECTION OF 2DFGRS GALAXIES

In measuring the radio properties of 2dFGRS galaxies in our pilot survey, we restricted our radio image to a lowest RMS sensitivity of 1 mJy, the outermost contour in Fig. 3. This is necessary as to limit the uncertainty in the primary beam corrections of our radio image. The total area to a 1 mJy detection limit is  $\sim 3$  deg $^2$ . Fig. 5 shows the variation of survey area as a function of  $1\sigma$  sensitivity.

Based on the final 2dFGRS data release, a total of 392 2dFGRS objects lie within the 1 mJy-region of the ATCA

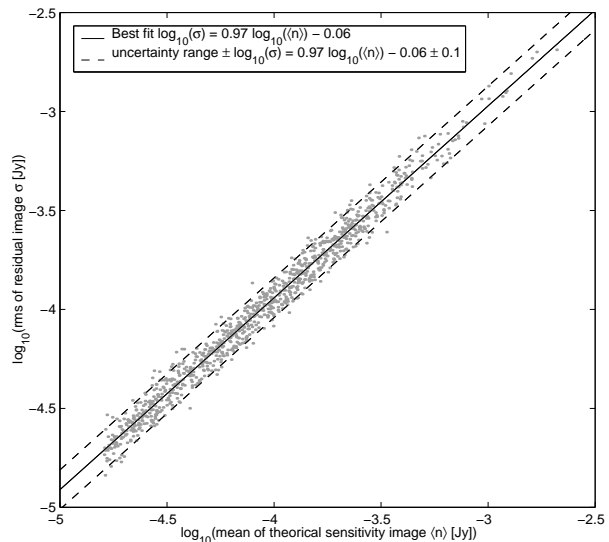


**Figure 4.** Plot of residual image rms against theoretical sensitivity image mean, with a best-fitting line (solid) and approximated range of uncertainty (dashed-lines).

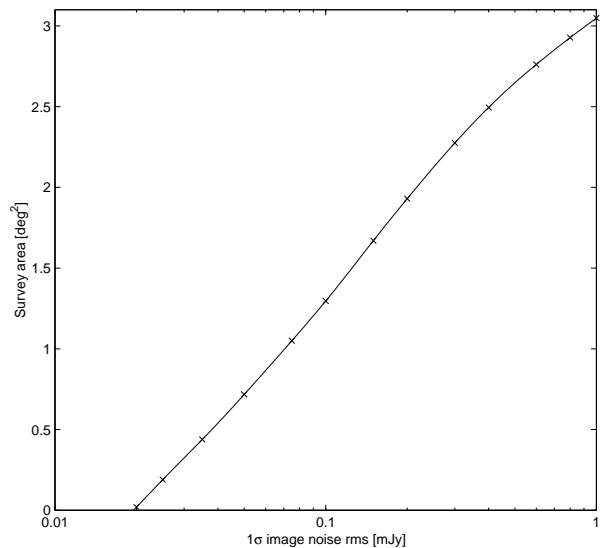


**Figure 5.** Survey area as a function of  $1\sigma$  RMS noise level. The solid line is a cubic spline interpolation of the data.

mosaic. Of these, 27 have reliable ( $Q \geq 3$ ) low-redshift spectra ( $z \leq 0.001$ ), they are stars and have been excluded from further analysis. The spectra of the remaining 365 objects have been visually classified by author BC and cross-checked by author EMS. We adopted the visual classification scheme used by Sadler et al. (2002) a subset of which were also classified by Jackson & Londish (2000) using diagnostic emission-line ratios. The spectra were classified as AGN galaxies with (1) *abs*: absorption line spectra, (2) *em*: emission-line spectra with dominant forbidden lines (e.g. [OIII]), or (3) *a+e*: combined absorption and emission line spectra, or as star-forming galaxies with (4) *SF*: emission-line spectra with dominant recombination lines (e.g. H $\alpha$ ), or as un-classifiable objects (5) *???*: objects with spectra

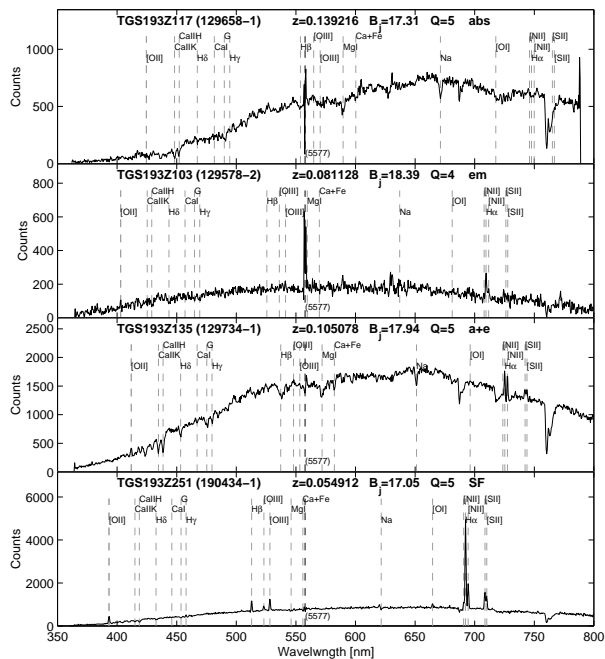


**Figure 6.** Examples of 2dFGRS spectra, classified from the top as (1) *abs*, (2) *em*, (3) *a+e*, and (4) *SF*. See §3 for details.

which are too noisy or otherwise un-classifiable. Note that due to aperture effects of fiber spectroscopy, a spectra classified as *abs* or *a+e* may depend on the redshift of the galaxy (e.g. see Sadler et al. 2002, their Fig.4 and §3.4). Fig. 6 exhibits sample 2dFGRS spectra in classes (1)–(4) from top to bottom.

We aim to determine the radio flux density or an upper limit at each 2dFGRS source position. For the brighter radio sources, this can be done by cross-matching a radio source catalogue to the 2dFGRS catalogue. However, since the optical source positions are known we can explore potential low signal-to-noise (S/N) detections by examining the statistical outcomes of source fitting at the known optical positions. Our strategy for cross-identification when the optical positions are known employs the AIPS procedure VSAD to catalogue radio sources with peak flux density  $\geq 5$  times the local image noise rms, and the MIRIAD procedure IMFIT to examine the statistical properties of pixels near the optical sources. Estimated uncertainty in the flux density measurements by the two source fitting programs have been derived using Monte-Carlo simulations, the results are presented in Appendix I.

We deploy VSAD for multiple Gaussian fitting within regions of  $\sim 3$  beam areas, centred in the previously determined CLEAN boxes and adopting a peak flux density cutoff of 3 times the local RMS noise determined as explained in §2.2. The resulting  $3\sigma$  peak flux density list is filtered to produce a radio source list with peak flux densities exceeding the local  $5\sigma$  level and inspected visually to reject obvious spurious fits. This radio source catalogue, containing 326 single components and 2 paired sources, is then cross-matched with the 365 2dFGRS positions. To determine the optimal search radius for cross-matches, we consider Fig. 7 which shows the number of matches (“o” with  $\sqrt{N}$  Poisson er-

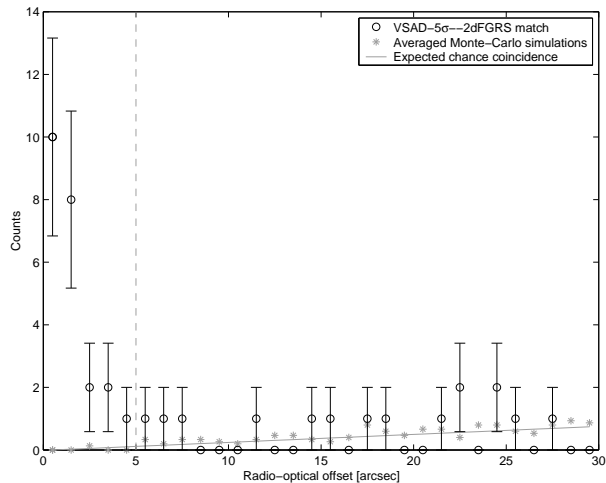


**Figure 7.** The differential matches of radio-2dFGRS sources as a function of radio-optical offset, shown with Poisson errorbars ( $\sqrt{n}$ ). Also shown are averaged Monte-Carlo test results and the solid line shown the expected chance coincidence level, assuming radio sources are uniformly distributed.

rorbars) inside consecutive concentric annuli centred at the optical position. Monte-Carlo techniques were used to determine the level of chance coincidence in the case of variable survey sensitivity. The Monte-Carlo results (“\*”-symbols) agreed well with the expected chance coincidence (dotted-line in Fig. 7) calculated for a uniform radio source density. Fig. 7 shows that beyond a radio-optical offset of about 4–5 arcsec, the rate of radio-2dFGRS cross-matches overlaps with that expected from chance coincidence. Matches with offsets up to 5 arcsec are accepted as automatic identifications, but we visually inspect matches up to 15 arcsec offset to uncover special cases.

Of the 365 2dFGRS positions, we found 23 identifications with radio-optical offsets smaller than 5 arcsec, and 3 positions with 5–10 arcsec offsets which were all accepted after visual inspection. The 2 matches with offsets 10–15 arcsec were rejected as identifications.

For each 2dFGRS position without a radio match, the MIRIAD task IMFIT was used to attempt a least-squares fit of the radio point spread function at the optical position. Although the fitting algorithm is understandably unstable, fits converged for 65 cases out of the remaining 339 optical positions, with a fitted peak flux density greater than the estimated local RMS noise ( $1\sigma$ ). Of these, 9 having a peak flux density  $\geq 3\sigma$  are reported as flux density measurements. The 56 with fits below  $3\sigma$  are characterised as upper limits. For the remaining 274 optical positions with unsuccessful IMFIT results (divergent fits or fitted flux density  $\leq 1\sigma$ ) we report a flux density of zero, and specify the estimated local noise as the radio upper limit.

We developed a *glissh*-script to generate image overlays using methods in the VIEWER-tool of AIPS++. Red 2<sup>nd</sup> epoch Digitized Sky Survey (DSSII-red) images<sup>2</sup> were overlaid with radio contours at each of the 365 2dFGRS objects.

<sup>2</sup> DSS images obtained from the *Canadian astronomy data centre*, at: <http://cadwww.dao.nrc.ca/dss/>

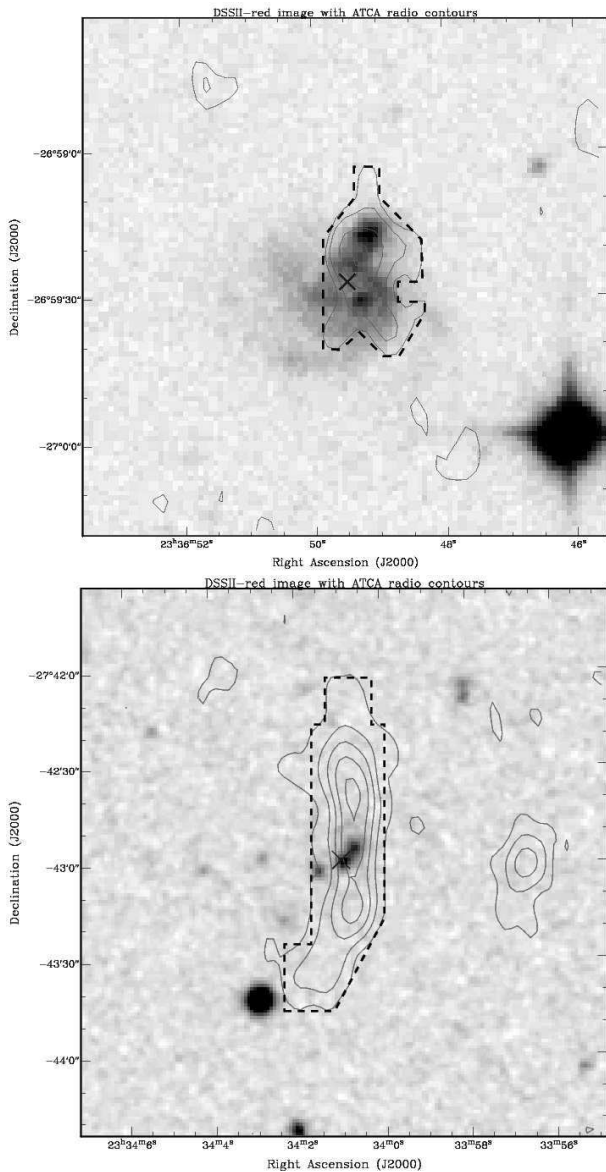


**Figure 8.** DSSII-red image overlaid with (top) radio contours at 2, 3, 5, and  $7 \times \sigma = 474 \mu\text{Jy}$  and (bottom) radio contours at 2, 6, 11, 17, and  $24 \times \sigma = 358 \mu\text{Jy}$ . The dashed outline marks the region used to determine the radio flux density and the cross marks the 2dFGRS position.

These images led us to accept all 3 matches with radio-optical offsets between 5–10 arcsec, and also revealed two objects whose radio emission was extended and required pixel summation to determine the integrated flux densities. DSSII-red images of these objects are displayed in Fig. 8, overlaid with radio contours. The dashed-outline in Fig. 8 shows the region used to determine the radio flux density and the cross marks the corresponding 2dFGRS object position.

### 3.1 ATCA-2dFGRS data-table

We publish here the radio flux density measurement or upper-limits of the 365 2dFGRS objects within our ATCA

radio survey region. Table 3 shows page 1 of the full data table. This catalogue is sorted on right ascension, and the structure of the table is as follows:

- Columns 1 & 2:* 2dFGRS position (J2000);
- Column 3:* 2dFGRS object name;
- Column 4:* 2dFGRS redshift;
- Column 5:* final  $B_j$  magnitude used in 2dFGRS;
- Column 6:* 2dFGRS redshift measurement quality;
- Column 7:* visual spectral classification;
- Column 8:* fitting method used to determine the radio flux;
  - (1) VSAD- $5\sigma$  match;
  - (2) IMFIT  $\geq 3\sigma$  match;
  - (3) IMFIT 1 – 3  $\sigma$  match;
  - (4) local noise upper limit;
  - (5) pixel sum;
- Columns 9 & 10:* VSAD- $5\sigma$  fitted radio position;
- Column 11:* estimated VSAD fitted positional uncertainty in arcsec, see Appendix I;
- Column 12:* radio-optical angular separation;
- Columns 13 & 14:* peak & integrated radio flux density determined using the corresponding fitting method;
- Columns 15 & 16:* percentage & actual radio flux density uncertainty<sup>3</sup>, see Appendix I;
- Column 17:* estimated local noise, see §2.2;
- Column 18:* radio signal-to-noise ratio of the detection.

### 3.2 Summary and comparison of results

Of the 365 2dFGRS objects with  $z > 0.001$ , 316 have reliable spectral classification, with 176 and 140 classified as AGNs and star-forming galaxies, respectively. The remaining 49 objects were unclassified, having either a low quality flag ( $Q < 3$ ) or noisy spectra.

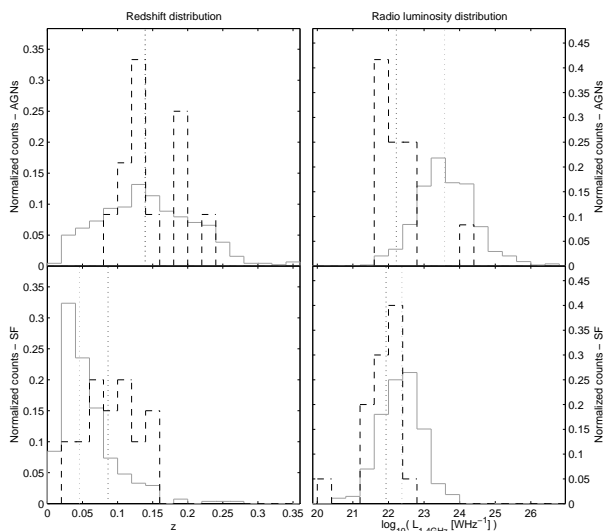
Of the 35/365 (9.6%) radio detections (measured radio flux density exceeding  $3\sigma$ ) of these galaxies, 12 were classified as AGNs, 20 as star-forming galaxies, and 3 were unclassified. Table 4 presents a summary of the radio detection rate of AGNs and star-forming galaxies in 2dFGRS for the current survey and those identified with NVSS sources by Sadler et al. (2002). It is difficult to compare the NVSS and ATCA values in view of the varying sensitivity in the ATCA survey, but they do reveal a rise in the detection rate with deeper radio sensitivity, especially for the star-forming population.

Fig. 9 shows the redshift and radio luminosity distributions of the radio-identified 2dFGRS sources associated with AGN and star-forming populations. To facilitate comparison, each distribution were normalised by the total of the distribution. Note that the narrow range of radio luminosities found in the ATCA sample is a selection effect owing to the combination of optical-radio survey cutoffs and the relatively small surveyed area. The sub-mJy ATCA survey detects an increasing proportion of lower-luminosity AGNs lying over a redshift range similar to that of sources detected above 2.7 mJy, as well as an increasing proportion of higher-redshift star-forming galaxies having a mean luminosity slightly lower than the NVSS sample. This implies

<sup>3</sup> When the local noise exceeds the fitting uncertainty, the larger value was used.

**Table 4.** ATCA-2dFGRS summary.

	2dFGRS	ATCA detection	NVSS detection
z-unreliable	49	3 (6.1%)	—
AGN	176	12 (6.8%)	~ 1.8%
SF	140	20 (14%)	~ 1.1%
Total	365	35 (9.6%)	~ 1.5%
AGN:z <sub>med</sub> (sd)		0.14 (0.046)	0.14 (0.16)
SF:z <sub>med</sub> (sd)		0.086 (0.037)	0.046 (0.040)
AGN:log <sub>10</sub> (L <sub>1.4 GHz</sub> ) <sub>med</sub> (sd)		22.22 (0.69)	23.58 (0.81)
SF:log <sub>10</sub> (L <sub>1.4 GHz</sub> ) <sub>med</sub> (sd)		21.93 (0.47)	22.38 (0.58)



**Figure 9.** Redshift (left-column) and radio luminosity (right-column) distributions for AGNs (top-row) and star-forming galaxies (bottom-row) of 2dFGRS sources identified with this current radio survey (dashed-line-histogram) and NVSS sources (solid-line-histogram) from Sadler et al. (2002). The two vertical dotted-lines in each plot shows the median of the distributions, the actual values are listed in Table 4.

that a sub-mJy radio survey of the 2dFGRS will better reveal the population in the faint end of the AGN and star-forming galaxy radio luminosity function, and enable more reliable determination of the evolution of the star-forming population to  $z \approx 0.1$  (radio limited, 50  $\mu$ Jy) and the AGN population to  $z \approx 0.3$  (optical limited).

#### 4 RADIO LUMINOSITY FUNCTION

In this section we describe the construction of the total radio luminosity function (RLF) and the corresponding contributions by the AGNs and star-forming (SF) populations for our ATCA-2dFGRS sample. We have used the traditional  $1/V_{max}$  method of Schmidt (1968) to derive the RLF, as described in §2 of Condon (1989). According to the combined optical and radio survey constraints we calculate, for each

source, the maximum detectable redshift range  $[z_{min}, z_{max}]$ . Adopting the Einstein-de-Sitter model, the maximum detectable co-moving volume ( $V_{max}$ ) is given by:

$$V_{max} = 16\pi \left(\frac{c}{H_0}\right)^3 \int_{z_{min}}^{z_{max}} \omega(z) \frac{[1 - (z+1)^{-1/2}]^2}{(z+1)^{3/2}} dz, \quad (1)$$

where  $\omega(z)$  is the fraction of the surveyed solid angle at redshift  $z$ . The adopted optical survey limit is  $14.0 < b_J < 19.4$ . (Colless et al. (2001)), constant throughout the survey. The radio detection limit varies across the radio mosaiced region (see Fig. 3), and is set at  $3\sigma$ . A cubic spline interpolation of the relation shown in Fig. 5 provides an estimate of  $\omega(z)$  for any particular source, and  $V_{max}$  is obtained via numerical integration of equation 1 following the method described in §2(d) of Avni & Bahcall (1980). Similarly, we can calculate the detectable co-moving volume of each source ( $V$ ). The ratio  $V/V_{max}$  of a randomly distributed sample is expected to be uniform in the interval  $[0,1]$ , and the mean ( $\langle V/V_{max} \rangle$ ) should be  $\sim 0.5$ .

Our sample comprises 35 ATCA-2dFGRS sources which satisfy the survey limits stated above. Three without reliable redshifts are excluded from the RLF calculations, but included through the incompleteness correction. To estimate the level of incompleteness of our ATCA-2dFGRS RLF, we examined galaxies in the 2dFGRS input catalogue that fall within the radio surveyed region but were not observed with 2dF. Only one of these “missing” 2dFGRS sources was identified with a  $\geq 3\sigma$  radio source, implying that this optically selected radio-sample is approximately 90% (32/36) complete.

The total RLF and contributions by the AGNs and SF galaxies are listed in Table 5, also listed are the  $\langle V/V_{max} \rangle$  values. While the SF galaxies in our sample seems to be uniformly distributed, the  $V/V_{max}$  values of the AGNs show a small but not significant increase and they are non-uniformly distributed (median( $V/V_{max}$ ) = 0.617). This might indicate some level of clustering or evolution in the AGN fraction within our sampled volume.

Presented in Fig. 10 is the total RLF of our ATCA-2dFGRS sample (\*-solid) along with values derived from the NVSS-2dFGRS sample of Sadler et al. (2002). The RLF separated into the populations of AGNs and SF galaxies of the two samples is shown in Fig. 11. The values and the plots have not been corrected for the 10% incompleteness since the effect ( $\log_{10}(1.1)$ ) is small. Our RLF agrees well with that of Sadler et al. (2002), within measurement uncertainty and the luminosity range sampled, due to the similar redshift range sampled. Although our median redshift for the star-forming galaxies are higher, with such a small sample we are not yet able to test for any significant differences with respect to other samples.

#### 5 RADIO-2DFGRS DETECTION RATE

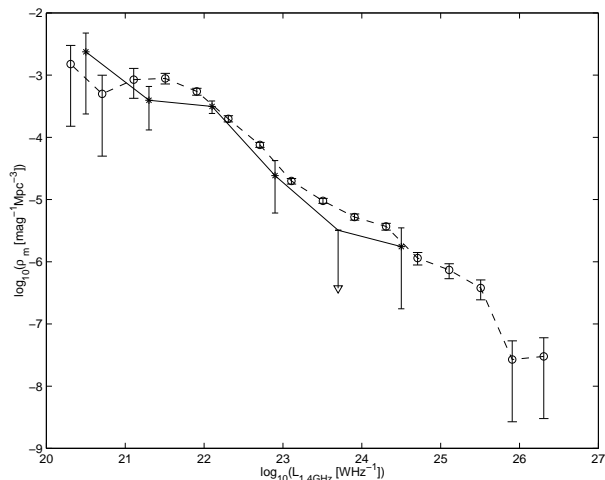
To explore the radio-2dFGRS detection rate at various radio detection limits, the radio survey was divided into four zones of sensitivity, starting from 25  $\mu$ Jy and doubling in four steps upwards. The four zones thus corresponded to  $3\sigma$  radio detection limits of 75, 150, 300 and 600  $\mu$ Jy. The number of 2dFGRS sources and radio detections above the  $3\sigma$  limit are counted in each zone, separated into three optical spectral



**Table 5.** ATCA-2dFGRS radio luminosity function.

$\log_{10}(L^\diamond)$	All galaxies		SF galaxies		AGNs	
	N	$\log_{10}(\rho_m^\heartsuit)$	N	$\log_{10}(\rho_m^\heartsuit)$	N	$\log_{10}(\rho_m^\heartsuit)$
20.5	1	$-2.62^{+0.30}_{-1.00}$	1	$-2.62^{+0.30}_{-1.00}$	-	-
21.3	5	$-3.40^{+0.22}_{-0.48}$	5	$-3.40^{+0.22}_{-0.48}$	-	-
22.1	23	$-3.50^{+0.09}_{-0.11}$	14	$-3.67^{+0.11}_{-0.15}$	9	$-3.99^{+0.13}_{-0.19}$
22.9	2	$-4.62^{+0.24}_{-0.60}$	-	-	2	$-4.62^{+0.24}_{-0.60}$
23.7	0	$\leq -5.49$	-	-	0	$\leq -5.49$
24.5	1	$-5.76^{+0.30}_{-1.00}$	-	-	1	$-5.76^{+0.30}_{-1.00}$
Total	32		20		12	
$\langle V/V_{max} \rangle$	$0.526 \pm 0.051$		$0.492 \pm 0.065$		$0.584 \pm 0.083$	

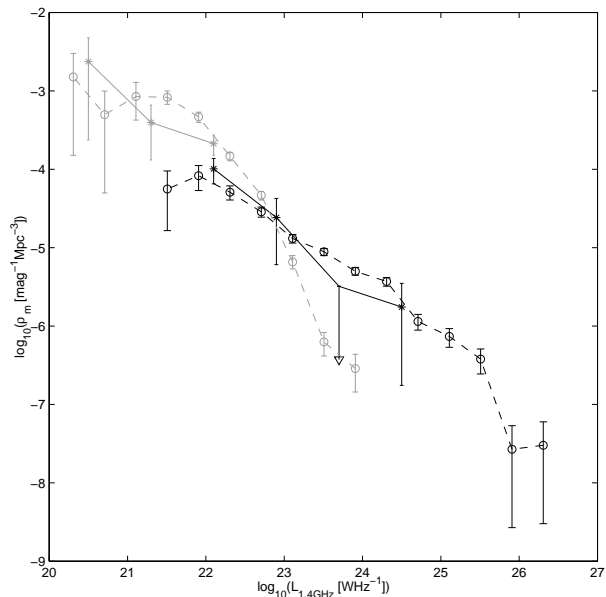
$\diamond$   $L_{1.4\text{GHz}}$  in [ $\text{WHz}^{-1}$ ]  
 $\heartsuit$   $\rho_m$  in [ $\text{mag}^{-1}\text{Mpc}^{-3}$ ]

**Figure 10.** Total radio luminosity functions for the 2dFGRS-NVSS sample of Sadler et al. (2002) ( $\circ$  dashed-line) and our 2dFGRS-ATCA sample ( $*$  solid-line).

classes: (i) star-forming (SF) galaxies, (ii) AGNs and (iii) no redshift (unknown). These counts are listed in Table 6, excluding the detections above the 2.8 mJy limit used in Sadler et al. (2002).

Our survey region has been specially selected to avoid bright radio sources, therefore the radio-2dFGRS detection rates calculated from our sample could be biased against identifications with bright sources. To overcome this possible bias, we have adopted the expected detection rate for sources above 2.8 mJy using the NVSS-2dFGRS results of (Sadler et al. 2002). Fig. 12 illustrates the proportion of 2dFGRS sources identified with radio sources as a function of radio survey sensitivity. This is calculated from the sum of the detection rates at the various radio detection limits listed in Table 6 and the corresponding detection rate from the NVSS-2dFGRS sample.

The plot shows an approximate 10-fold increase in the detection rate for a 10-fold improvement in radio detection sensitivity. This increase in detection rate would require a 100-fold increase in observing time. These results

**Figure 11.** Radio luminosity functions separated into the star-forming (lighter-colour lines) and the AGN (darker-colour lines) populations for the NVSS ( $\circ$  dashed-line) and ATCA ( $*$  solid-line) samples.

are broadly consistent with the estimates made in §2, using our observing strategy, we can obtain a sample evenly distributed in numbers of identifications, independent of the additional constraint imposed by 2dFGRS optical selection, across all radio flux densities.

## 6 LARGE SCALE RADIO SURVEY

Owing to the enormous time investment in acquiring large optical-spectroscopic redshift surveys such as that by 2dF makes it even more valuable to fully exploit its potentials. A large scale radio follow-up survey of the 2dF sources will fill a significant gap in the available data on faint radio sources. Existing radio-optical spectroscopic studies have been based on either (i) bright, large-scale radio surveys (FIRST<sup>4</sup>, NVSS and SUMSS<sup>5</sup>) that are cross-correlated with catalogued optical data (implying that the identified optical galaxies are also bright) or (ii) deep radio surveys made over small areas (such as: PDS<sup>6</sup>, HDF<sup>7</sup> and HDFS<sup>8</sup>) with pointed optical spectroscopy of selected optical IDs. Studies of type (i) have given radio-optical data on  $\sim 4000$  and  $\sim 1000$  nearby galaxies from the UGC-NVSS (Condon et al. 2002) and 2dF-NVSS (Sadler et al. 2002) & 2dF-FIRST (Magliocchetti et al. 2000), with  $z < 0.1$  and  $z < 0.3$ , respectively. Studies of type (ii) (which is very ex-

<sup>4</sup> Very Large Array-Faint Images of the Radio Sky at Twenty-centimeters (Becker, White & Helfand 1995).

<sup>5</sup> Sydney University Molonglo Sky Survey (Bock, Large & Sadler 1999).

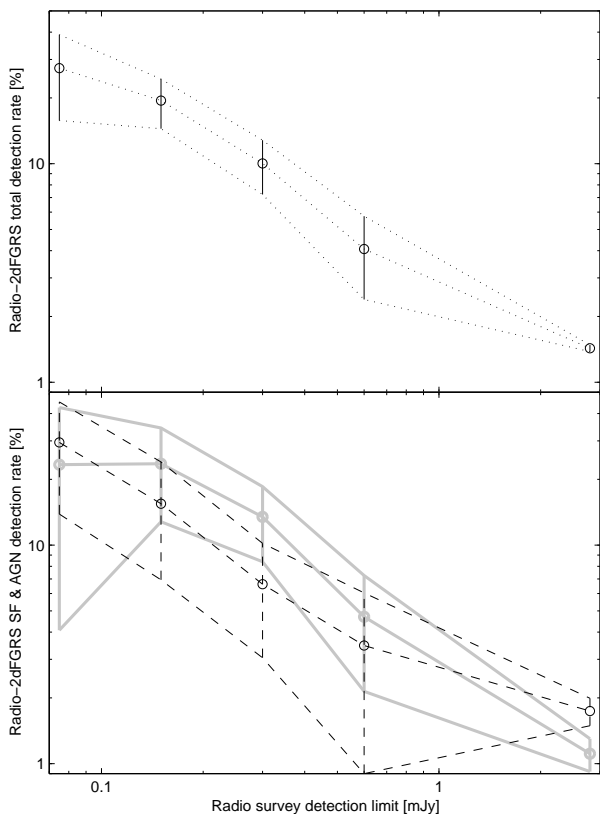
<sup>6</sup> Phoenix Deep Survey (Hopkins et al. 1998).

<sup>7</sup> Hubble Deep Field (Richards et al. 1998).

<sup>8</sup> Hubble Deep Field South (Norris et al. 2001)

**Table 6.** Radio-2dFGRS identification counts at the corresponding  $3\sigma$  radio limit up to the 2.8 mJy limit used in Sadler et al. (2002).

Radio $3\sigma$ limit (mJy)	Area (deg <sup>2</sup> )	Number of 2dFGRS galaxies				Number of radio identifications			
		Total	SF	AGNs	unknown	Total	SF	AGNs	unknown
0.075 – 2.8	0.19	27	8	17	2	7	2	5	–
0.150 – 2.8	0.72	100	43	45	12	18	10	6	2
0.300 – 2.8	1.30	163	73	74	16	14	10	4	–
0.600 – 2.8	1.93	227	97	101	29	6	4	2	–

**Figure 12.** Radio-2dFGRS detection rate at various radio detection limits. The lines interpolate the detection rate with Poisson errors for: *top-panel* – the total-detection rate (dotted-line); *bottom-panel* – detection rates of star-forming galaxies (solid-line) and the AGNs (dashed-line). Note: (1) the detection rate at 2.8 mJy is from the NVSS-2dFGRS sample of Sadler et al. (2002), (2) the detection rates above 2.8 mJy are the *sum* of the corresponding NVSS-2dFGRS detection rate and the values shown in Table 6, see text for details.

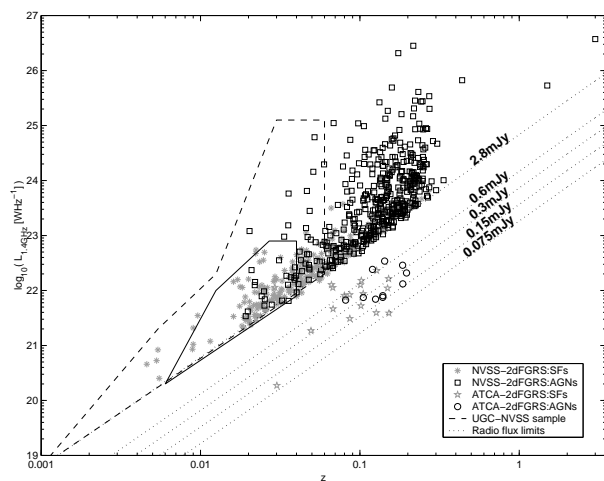
pensive of telescope time) has to date provided radio-optical data on fewer than 300 galaxies, at redshifts up to  $z \sim 1$ .

Fig. 13 displays the radio-detected 2dFGRS objects in the current survey and those in 2dF-NVSS. Also shown are dashed lines tracing out the UGC-NVSS sample, and a solid line delineating the main concentration of UGC-NVSS data points (predominately star-forming galaxies). It is clear that mJy radio surveys are only capable of properly sampling the full range of radio luminosities for the SF and AGN populations up to  $z \sim 0.01$  ( $L_{1.4\text{GHz}} \gtrsim 10^{21.5} \text{ WHz}^{-1}$ ). Whereas, even though the ultra-deep radio surveys can provide radio

luminosity sampling to very high redshifts ( $z \geq 1$ ), the problems lies in that pencil beam surveys (i.e. small survey area of typically a few square arcmin up to a few square degrees) are not ideal to sample galaxy evolution. There are inherent problems in small area surveys associated with clustering, cosmic variance, and the complex selection effects will be both difficult to model and correct for. A large area sub-mJy radio surveys of 2dFGRS sources with a varying sensitivity will link together the existing surveys and provide the required sample of the ‘normal’ population of sources in the intermediate redshift ranges up to  $z \sim 0.03$ -0.04. An investigation of possible systematic source flux differences between our ATCA survey and those in the NVSS, we present, in Appendix II, flux comparison of sources found common in the two surveys within our mosaiced region.

Sadler et al. (2002) estimate that approximately 4,000 radio-optical identifications will be found when the full 2dFGRS is correlated with the NVSS catalogue (Jackson et al. 2003, in preparation). Using the detection rates measured with our pilot study, we can now estimate the survey sensitivity and the total survey area (i.e. observing time) required to provide a set of radio IDs that is complete to a given radio luminosity and redshift. Computed in (Table 7) is the required observing time and the number of expected optical-radio identifications for a survey with three levels of sensitivity and survey area. The three adopted  $3\sigma$  sensitivity levels form a bridge between existing surveys, the poorest sensitivity level at 0.6 mJy being approximately half of the FIRST limit (the FIRST limit is approximately half of NVSS limit) while the best sensitivity level of 0.15 mJy is about half as good as that of PDS.

Employing a nested mosaicing technique the survey plan outlined in Table 7 will require a total of about 60–70  $\times$  12 hour observing sessions. The survey will image about 100 deg<sup>2</sup> of sky, making over 1000 radio/optical identifications. This number is required to address the important problem of constraining the cosmic evolution of the radio spectral power density of star-forming galaxies. The UGC-NVSS sample has provided a very precise measurement of the local ( $z \sim 0.01$ ) star formation density, presenting a local reference and has hinted at intriguing cosmic evolution of this quantity Condon et al. (2002). With favored evolutionary model in which the luminosity density rises as  $(1+z)^{3\pm 1}$ , the predicted increase of star formation rate density is  $\sim (30 \pm 10) \%$  at  $z \sim 0.1$ . With a sample size of 1000, divided into ten luminosity bins for deriving the redshift-dependence of the star formation density, producing a measurement uncertainty of  $\sim 10\%$ . This would be sufficient in distinguishing between various models for the cosmic evolution of the star formation density, providing a measure potentially superior



**Figure 13.** Plot of radio luminosity against redshift, for our ATCA-2dFGRS ( $3\sigma$ ) detections along with the NVSS-2dFGRS ( $\sim 5\sigma$ ) sample. The dashed-line traces out the UGC-NVSS ( $\sim 5\sigma$ ) sample, the solid-line shows the main concentration of data points (predominately star-forming galaxies). The dotted-lines shows various flux density limits.

to the traditional estimates via optical emission-line measurements or ultra-violet photometry which are unavoidably biased by dust extinction.

## ACKNOWLEDGMENTS

We thank the 2dFGRS team for data access prior to the public release.

We thank R.J. Sault for helpful advice regarding data reduction and joint deconvolution techniques. We also wish to thank M. Marquarding for helpful demonstration of the AIPS++ VIEWER-tool functionalities and answering many queries with respect to *glush*-scripting.

The Australia Telescope is funded by the Commonwealth of Australia for operation as a National Facility managed by CSIRO.

## REFERENCES

Avni Y., Bahcall J.N., 1980, ApJ, 235, 694.  
 Baars J.W.M., Genzel R., Pauliny-Toth I.I.K., Witzel A., 1977, A&AS, 61, 99.  
 Becker R.H., White R.L., Helfand D.J., 1995, ApJ, 450, 559.  
 Benn C.R., Rowan-Robinson M., McMahon R.G., Broadhurst T.J., Lawrence A., 1993, MNRAS, 263, 98.  
 Bock D.C.-J., Large M.I., Sadler E.M., 1999, AJ, 117, 1578.  
 Biermann P., 1976, A&A, 295, 303.  
 Colless M., et al (the 2dFGRS team), 2001, MNRAS, 328, 1039.  
 Condon J.J., 1988, in Verschuur G.L., Kellermann K.I., eds, Galactic and Extragalactic Radio Astronomy, second edition. Heidelberg: Springer-Verlag, 1988, p.641.  
 Condon J.J., 1989, ApJ, 338, 13.  
 Condon J.J., 1992, ARA&A, 30, 575.

Condon J.J., 1997, PASP, 109, 166.  
 Condon J.J., Cotton W.D., Greisen E.W., Yin Q.F., Perley R.A., Taylor G.B., Broderick J.J., 1998, AJ, 115, 1693.  
 Condon J.J., Cotton W.D., Broderick J.J., 2002, AJ, 124, 675.  
 Franceschini A., Vercellone S., Fabian A.C., 1998, MNRAS, 297, 817.  
 Georgakakis A., Mobasher B., Cram L., Hopkins A., Lidman C., Rowan-Robinson M., 1999, MNRAS, 306, 708.  
 Gruppioni C., Mignoli M., Zamorani G., 1999, MNRAS, 304, 199.  
 Hill T.L., Heisler C.A., Norris R.P., Reynolds J.E., Hunstead R.W., 2001, AJ, 121, 128.  
 Ho L.C., 2002, ApJ, 564, 120.  
 Hopkins A.M., Mobasher B., Cram L., Rowan-Robinson M., 1998, MNRAS, 296, 839.  
 Jackson C.A. & Londish D.M., 2000, PASA, 17 (3), 234.  
 Laor A., 2000, ApJ, 543, L111.  
 Magliocchetti M., et al. (the 2dFGRS team), 2002, MNRAS, 333, 100.  
 Nagar N.M., Falcke H., Wilson A.S., Ulvestad J.S., 2002, A&A, 392, 53.  
 Norris R.P., Hopkins A., Sault R.J., Mitchell D.A., Ekers R.D., Ekers J., Badia F., Higdon J., Wieringa M.H., Boyle B.J., Williams R.E., 2001, in Cristiani S., Renzini A., Williams R.E., eds, Proc. of the ESO/ECF/STScI Workshop held at Garching, Germany, 2000. Deep Fields. Springer, p.135.  
 Prandoni I., Gregorini L., Parma P., de Ruiter H.R., Vetolani G., Wieringa M.H., Ekers R.D., 2000, A&AS, 146, 31.  
 Prandoni I., Gregorini L., Parma P., de Ruiter H.R., Vetolani G., Zanichelli A., Wieringa M.H., Ekers R.D., 2001, A&A, 369, 787.  
 Regan M.W., Thornley M.D., Helfer T.T., Sheth K., Wong T., Vogel S.N., Blitz L., Bock D.C.-J., 2001, ApJ, 561, 218.  
 Richards E.A., Kellermann K.I., Fomalont E.B., Windhorst R.A., Partridge R.B.M., 1998, AJ, 116, 1039.  
 Sadler E.M., et al (the 2dFGRS team), 2002, MNRAS, 329, 227.  
 Schmidt M., 1968, ApJ, 151, 393.  
 Steer D.G., Dewdney P.E., Ito M.R., 1984, A&A, 137, 159.  
 Taylor G.B., 2002, in The VLA Calibration Manual, on-line at <http://www.aoc.nrao.edu/~gtaylor/calib.html>  
 Veilleux S., 2001, in Tacconi L., Lutz D., eds, proceedings of a Workshop held at Ringberg Castle, Germany, 2000. Starburst Galaxies: Near and Far. Heidelberg: Springer-Verlag, 2001, p.88. Preprint (astro-ph/0012121).  
 Windhorst R.A., 1984, Ph.D. thesis, Univ. Leiden.

## APPENDIX I: SOURCE FITTING AND UNCERTAINTIES

In measuring the radio flux density associated with 2dFGRS sources, we have used two automatic radio source fitting packages: (1) the AIPS task VSAD, and (2) the MIRIAD task IMFIT. We first matched the optical source list to a radio catalog generated with VSAD, of bright ( $\geq 5\sigma$ ) radio sources. For positions without a bright radio counterpart, we used IMFIT to determine radio upper-limits by fitting a beam

**Table 7.** Sample observing plan.

(1) Area (deg <sup>2</sup> )	(2) # pointing	(3) 3 $\sigma$ (mJy)	(4) ID rate (%)	(5) time/field (min)	(6) # of 12hr observation	(7) #ID/deg <sup>2</sup>	(8) #ID below NVSS/deg	(9) Total #ID
98.0	1221	0.60	5	7.5	13	5.12	3.6	351
49.0	610	0.30	10	30.0	25	10.23	8.7	426
24.5	305	0.15	20	120.0	51	20.47	18.9	464

- (1) Area surveyed (in square degrees) to specified sensitivity.
- (2) Number of pointings needed to cover required area.
- (3) Radio 3 $\sigma$  ( $3 \times$  image noise rms) sensitivity limit.
- (4) Percentage of expected optical-radio identification rate, obtained from pilot study.
- (5) Amount of radio telescope time required to reach sensitivity limit per pointing.
- (6) Number of 12 hour observing sessions required to cover area.
- (7) Number of optical-radio identification expected per square degree.
- (8) Number of optical-radio identification expected per square degree inaccessible to NVSS.
- (9) Total number of optical-radio identification down to the sensitivity limit inaccessible to NVSS.

size elliptical Gaussians at the known optical positions. Following these techniques, we investigated the source fitting uncertainty with Monte-Carlo simulations.

Beam-size Gaussians were injected at randomly chosen positions into the residual image of the deep-CLEANed mosaic. To obtain an estimate of the source fitting accuracy as a function of fitted source strength<sup>9</sup> ( $\sigma_s$ ), a range of injected source strengths were used, corresponding to a signal-to-noise ratio up to 150  $\sigma$ . We first used VSAD to generate a 5 $\sigma$  radio source list, following the same procedures as we used in our study (see §3). The input position list is then matched against the 5 $\sigma$  radio source list to within 10 arcsec, while fitting with IMFIT at the known source position for those without a match.

Shown in Fig. 14 is the Monte-Carlo results for the VSAD fitted angular positional deviation from the input at various fitted source strengths. The solid-curve is a quadratic least-square fit to the logarithmic one-standard deviation binned values of the results. This curve bounds about 90% of the data points. For instance, for about 90% of the 5 $\sigma$  VSAD sources in our radio catalog, we expect to have a positional uncertainty of  $\lesssim 3$  arcsec.

The results of the Monte-Carlo simulations for the two source fitting packages are shown in Fig. 15. Plotted in linear-log scales is the fitted peak flux fractional difference  $dS/S = (S_{input} - S_{fitted})/S_{fitted}$ , as a function of source strength. The two solid curves are quadratic least-square fits to the one-standard-deviation level of  $\log_{10}(|dS/S|)$ . The upper and lower bounds were fitted separately to better represent the complex behavior of the source fitting algorithm in the presence of noise. The uncertainty has been set to a absolute minimum of 5% for strong sources. Overall, the estimated uncertainty bounds  $\gtrsim 90\%$  of the data. The deficit of data points with low fitted flux densities ( $dS/S < 0$ ) at faint source strengths is the well-known property of radio source fitting in the presence of noise, as described in Condon (1997).

For the VSAD results in our present work, we have made

<sup>9</sup> The fitted source strength ( $\sigma_s$ ) is defined as the ratio of the fitted peak flux density ( $S_{peak}$ ) to the estimated local noise ( $\sigma_n$ , see §2.2).

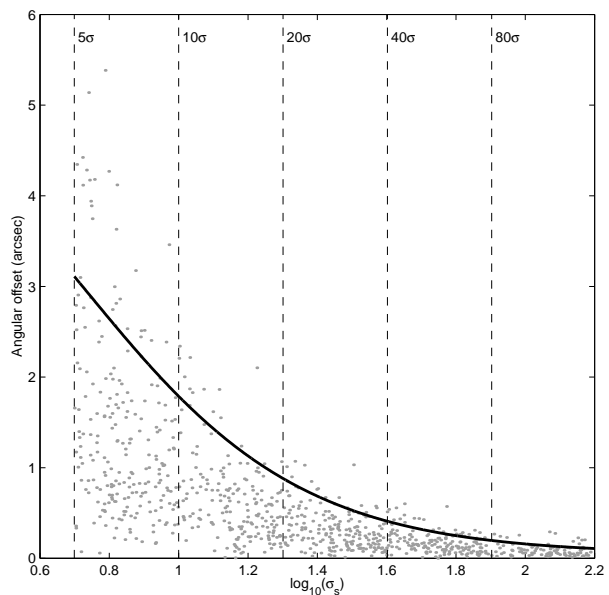


**Figure 14.** The angular separation between the input and fitted source position as a function of fitted source strength, in linear-log scales. The solid curves indicates the fitted estimate of the positional fitting uncertainty as a function of fitted source strength. The vertical dashed-lines denotes the various fitted signal-to-noise ( $\sigma$ ) level.

the assumption that the fractional uncertainty in fitted peak flux density is representative of the fitted integrated flux density.

## APPENDIX II: ATCA AND NVSS FLUX SCALE

Radio sources have an extremely wide range of luminosities and usually requires a combination of surveys at various sensitivity and aerial coverage to properly sample the radio population. In this section, we consider the possibility of combining radio data from a survey with the ATCA and the NVSS from the VLA. We compared the source flux density measured in our survey and those in NVSS. With

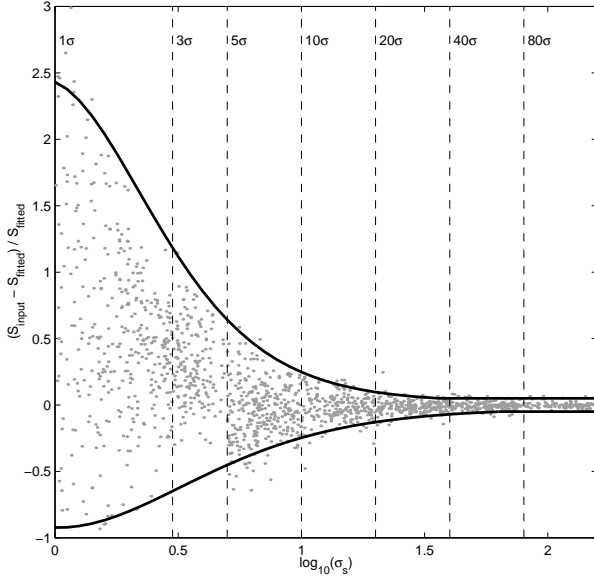


**Figure 15.** The fitted peak flux deviation as a function of fitted source strength for the Monte-Carlo simulations, in linear-log scales. The solid curves indicates the fitted estimate of the fractional source fitting uncertainty as a function of fitted source strength. The vertical dashed-lines denotes the various fitted signal-to-noise ( $\sigma$ ) level.

the on-line NVSS catalog browser<sup>10</sup> we extracted the 157 NVSS sources, brighter than 2.5 mJy, lying within our current ATCA-2dFGRS mosaic region. NVSS has a resolution of 45 arcsec and this is typically the minimum angular separation between sources in the NVSS catalog. With higher angular resolution, some NVSS sources are resolved in our ATCA survey. To locate these ‘decomposed’ sources, we matched the 157 NVSS positions to our 5 $\sigma$  VSAD list using a search radius of 45 arcsec, centred at the NVSS source positions. For matches with multiple components we represent the ATCA flux by simply adding the fitted integrated flux of the components. We used the NVSS flux uncertainty (provided with the catalog) and our estimated flux uncertainty (derived with Monte-Carlo simulations, see Appendix I) as a measure of the degree of deviation (the ‘sigma-level’) of the data from the perfect one-to-one correlation. For instance, a source with NVSS flux  $S_{\text{NVSS}} \pm \Delta_{\text{NVSS}}$  and corresponding ATCA flux  $S_{\text{ATCA}} \pm \Delta_{\text{ATCA}}$ , we defined the deviation ‘sigma-level’ ( $\Delta_\sigma$ ), such that, for  $S_{\text{NVSS}} > S_{\text{ATCA}}$ ,

$$S_{\text{NVSS}} - \Delta_\sigma \Delta_{\text{NVSS}} = S_{\text{ATCA}} + \Delta_\sigma \Delta_{\text{ATCA}},$$

or in general,

$$\Delta_\sigma = \left| \frac{S_{\text{ATCA}} - S_{\text{NVSS}}}{\Delta_{\text{NVSS}} + \Delta_{\text{ATCA}}} \right|.$$

We visually examined all NVSS positions with  $\Delta_\sigma \geq 1.5$  and those without an ATCA match. We found for a few extended sources, the Gaussian fitting method was inappropriate and we adopted the sum of the pixel values as the flux measurement. There are also a few cases where the source structure

**Table 8.** ATCA–NVSS cross identification results.

Type	$\Delta_\sigma: \leq 1$	1–2	2–3	>3	Total	
(1)	72	29	7	0	108	(69%)
(2)	16	3	0	0	19	(12%)
(3)	1	0	0	0	1	(<1%)
(4)	7	2	0	1	10	(6%)
(5)	9	0	0	0	9	(6%)
(6)	0	0	6	4	10	(6%)
Total	105 (67%)	34 (22%)	13 (8%)	5 (3%)	157	
(7)	0	6	1	2	9	

- (1) Single ATCA component match.
- (2) Double ATCA components match.
- (3) Triple ATCA components match.
- (4) Extended structure requiring pixel summation.
- (5) Special cases.
- (6) Undetected in ATCA.
- (7) ATCA sources  $\geq 2.5$  mJy without NVSS match ( $\sim 6\%$ ).

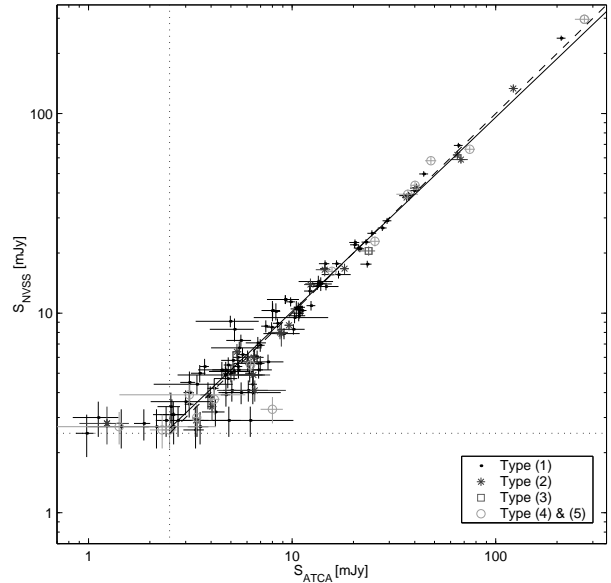


**Figure 16.** The NVSS and ATCA flux measurements of sources matched within our survey region. The different types of symbols denoted in the figure correspond to the matched-types listed in Table 8. The solid line is the least square fit to the data, the gashed-line is the one-to-one correlation between NVSS and ATCA fluxes. The dotted lines notes the 2.5 mJy NVSS limit adopted.

required some special care. The results of the cross identification process is listed in Table 8 and plotted in Fig. 16. From this small study, we did not observe any signs of significant systematic differences between the two radio surveys, in particular, there do not seem to be any systematic loss of total radio flux density in the ATCA survey for intrinsically extended sources (i.e. sources resolved by ATCA).

<sup>10</sup> <http://www.cv.nrao.edu/nvss/NVSSlist.shtml>

